Article

Oxygen vacancy clusters in bulk cerium oxide and the impact of gold atoms

Au ceria catalyst

Au   Au
150 °C
CO
ceria
600 °C

● oxygen vacancy   ● oxygen   ● cerium

Alessandro Longo, Alessandro Mirone, Emmanuelle De Clermont Gallerande, ..., Lucia Amidani, Stavros A. Theofanidis, Francesco Giannici

alessandro.longo@esrf.fr (A.L.)
alessandro.mirone@esrf.fr (A.M.)

Highlights

Random vacancies in ceria bulk aggregate in a cluster upon carbon monoxide treatment at 600°C

Gold catalyst random vacancies aggregate in a linear cluster upon carbon monoxide treatment at 150°C

Cluster formation is monitored by studying the oxygen K-edge with X-ray Raman spectroscopy

Ceria is pivotal in catalysis, as it forms and utilizes oxygen vacancies in redox reactions. Here, Longo et al. observe bulk oxygen vacancy aggregation, and demonstrate that the presence of gold effectively mitigates bulk oxygen vacancy aggregation, enhancing catalytic performance.

Cell Reports
Physical Science

Article

Oxygen vacancy clusters in bulk cerium oxide and the impact of gold atoms

Alessandro Longo,[1,2,7,*] Alessandro Mirone,[1,*] Emmanuelle De Clermont Gallerande,[1] Christoph J. Sahle,[1] Maria Pia Casaletto,[2] Lucia Amidani,[3,4] Stavros A. Theofanidis,[5] and Francesco Giannici[6]

SUMMARY

Ceria is important for catalysis due to its ability to form and utilize oxygen vacancies during redox reactions. Understanding the dynamic formation of the oxygen vacancies has contributed to the development of efficient catalytic processes. Here, we demonstrate the presence of oxygen vacancy clusters in the bulk of ceria and gold/ceria catalysts upon anaerobic carbon monoxide oxidation and describe their interplay with the orbital hybridization of Ce^{3+} 4f and 5d states. Observations are made using *in situ* X-ray Raman scattering spectroscopy at O K- and Ce $N_{4,5}$-edges and *in situ* X-ray diffraction. These, combined with multiplet calculations, allow detection of the formation of Ce^{3+} in gold/ceria upon low temperature carbon monoxide oxidation. The modifications observed at the O K-edge reflect the rearrangement of the bulk oxygen sublattice. Density-functional theory calculations show vacancy ordering in the bulk, and explain modifications at the O K-edge, involving the hybridization of the Ce 4f and 5d and O 2p orbitals.

INTRODUCTION

The CO oxidation reaction in anaerobic conditions on reducible oxides is one of the most widely studied processes in heterogeneous catalysis. This apparently simple reaction is paradigmatic and relevant for understanding a number of important processes from the water-gas shift used for the production of hydrogen to the oxidation of hazardous volatile organic compounds.[1–9]

Among the wide variety of reducible oxides used as a support, ceria (CeO_2) remains unique due to its remarkable oxygen storage capacity and redox properties.[1,2] These originate in the easy switching between Ce^{4+} and Ce^{3+}, creating oxygen vacancies that are easily accommodated in the anion sublattice.[1–11] Ceria therefore enables reduction and oxidation reactions via the uptake and release of oxygen. The high activity of gold nanoparticles supported on ceria toward the oxidation of CO to CO_2 has been explained by the increasing of the vacancy formation process, which is ultimately linked to an improved oxygen release.[12] In this scheme, the surface oxygen atoms are directly involved in the oxidation and thus result in the formation and bulk migration of lattice oxygen vacancies.[13–15] The adsorption and reaction are expected to occur especially in the peripheral sites located at the metal-support boundary.[13,16] The formation of a Schottky junction at the interface with the Au particles might also enhance the formation of oxygen vacancies.[17]

[1]European Synchrotron Radiation Facility, Grenoble, France

[2]Istituto per lo Studio dei Materiali Nanostrutturati - Consiglio Nazionale delle Ricerche, Palermo, Italy

[3]The Rossendorf Beamline at the European Synchrotron Radiation Facility, Grenoble, France

[4]Helmholtz-Zentrum Dresden-Rossendorf, Institute of Resource Ecology, Dresden, Germany

[5]AristEng S.à r.l., 77, Rue de Merl, L-2146 Luxembourg City, Luxembourg

[6]Dipartimento di Fisica e Chimica "Emilio Segrè", Università di Palermo, Palermo, Italy

[7]Lead contact

*Correspondence:
alessandro.longo@esrf.fr (A.L.),
alessandro.mirone@esrf.fr (A.M.)

https://doi.org/10.1016/j.xcrp.2023.101699

CellPress
OPEN ACCESS

Cell Reports
Physical Science
Article

The formation of oxygen vacancies is connected to an electronic change in the ceria support according to the following defect-chemical equation: $O^X_O = V^{\bullet\bullet}_O + 2e^- + 1/2\, O_2(g)$, where O^X_O is a lattice oxide ion, and $V^{\bullet\bullet}_O$ is an oxygen vacancy carrying a relative double-positive charge.[17–19] When lattice oxygen (formally O^{2-}) is removed during the CO oxidation step, the two excess electrons can be accommodated by the reduction of support cations,[13,14,18] and localize on empty f states of the Ce^{4+} ions resulting in the change of valence to Ce^{3+} due to small polaron hopping.[19]

In this context, the following critical points remain open questions in current catalysis research on ceria based materials: (1) the oxygen vacancy formation mechanism, (2) the electronic modifications at the Ce sites, and (3) how the latter two factors evolve during CO oxidation.[19,20] Several fundamental studies have been performed in the last two decades on how the oxygen vacancies are created and organized in ceria, especially at the surface and what are the accompanying electronic modifications. Esch et al. described how oxygen vacancies, immobile at room temperature, cluster together at higher temperatures to form linear aggregates, which are the dominant defects on reduced ceria (111) surfaces.[19] These clusters expose only Ce^{3+} ions to the reaction gas, while the sites adjacent to these aggregated defects are Ce^{4+}.[21–23] Remarkably, the subsurface vacancies facilitate catalysis, since they enable a further release of surface oxygen, and stabilize the formation of linear oxygen vacancy clusters. Torbrügge et al., analyzing a highly defective system in cryogenic conditions, studied the interaction of surface and subsurface oxygen vacancies, which results in open linear defect clusters.[24] To complete this scenario with electronic considerations, Jerratsch et al. evidenced the splitting of the filled Ce^{3+} f levels due to the variation in their chemical environment occurring with the vacancy formation.[25] Several other theoretical studies were concerned in particular with the mutual position of Ce^{3+} and oxygen vacancies in the lattice.[20,26–31]

So far, the investigations of oxygen vacancy organization in clusters have been focused on the existence of superficial or sub-superficial oxygen defects. The electronic modifications occurring in the bulk of the ceria support have remained much less investigated and reported mostly in theoretical works.[26–33]

Recently, the possibility to locate the vacancies formed in the bulk of ceria has received renewed attention. Mehmood et al., using photoelectron techniques, strived to provide a quantitative determination of the different oxygen vacancy concentrations, decoupling them into surface-filled, subsurface-unfilled, and bulk contributions.[32] Recent neutron studies have also revealed a partially reduced ceria phase with long-range ordering of oxygen vacancies.[33,34]

The evolution of oxygen vacancies in the bulk of ceria also upon thermal and chemical treatments is still rarely investigated, and there remain fundamental and unaddressed questions. Clarifying the possible formation of oxygen vacancy clusters in the bulk represents a big leap in the understanding of the working conditions of oxidation reactions on ceria catalysts.

Since the oxygen vacancies and the formation of Ce^{3+} occur concurrently, some authors exploited the Ce L_3-edge as a probe for oxygen defectivity. In this respect, both static and *in situ* X-ray absorption near-edge spectroscopies (XANES), possibly within high-energy-resolution fluorescence detection (HERFD) mode, have been used. Especially for the low-resolution experiments, the mixing of the f and d orbitals of Ce^{3+} makes the spectral variation, which is mainly characterized by the Ce^{4+} features, hard to recognize, and the detection of Ce^{3+} remains challenging and far from
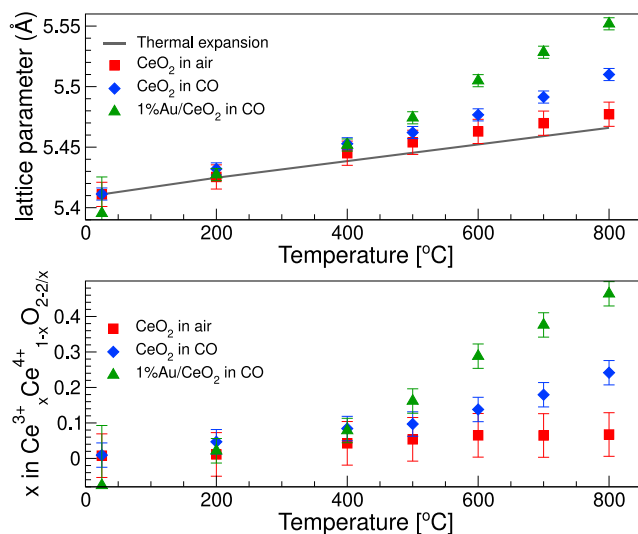
Figure 1. In situ XRD results

Upper panel: Thermal evolution of cubic lattice parameter of CeO_2 up to 800°C CeO_2 in air (red) and in CO (blue), and 1%Au/CeO_2 in CO (green): the effect of thermal expansion is shown as a black line. Lower panel: fraction of Ce^{3+} in CeO_2 in air (red) and in CO (blue), and in 1%Au/CeO_2 in CO (green). The error bars are obtained according to Rietveld analysis.

unambiguous. Ultimately, only an indirect information on the state of oxygen species can be obtained.[35–39]

In this study, we show that the electronic modifications of the anion sublattice induced by the oxygen vacancy formation in the bulk, can be unveiled by measuring the O K-edge via X-ray Raman scattering (XRS) spectroscopy on both ceria and Au/ceria during a CO oxidation reaction. XRS exploits hard X-rays to measure the K absorption edge of oxygen and the $N_{4,5}$-edges of cerium, avoiding the need for high vacuum and therefore circumventing the constraints of soft X-rays. Therefore, XRS offers the unique advantage to provide direct information on the bulk, usually inaccessible to valence-level spectroscopies.[40–42] Remarkably, we show here that the *in situ* measurements at the Ce $N_{4,5}$-edges provide a powerful tool to monitor the Ce^{3+} formation during the chemical treatment.

The *in situ* XRS measurements are modeled by combining *ab initio* density-functional theory (DFT) calculations and multiplet analysis. Exploiting the parallel information from *in situ* XRD to evaluate the total Ce^{3+} fraction,[43,44] a correlation of the modifications occurring in the oxygen sites of ceria bulk and the formation of vacancy clusters is established.

The combined information from experiments and modeling clarifies the oxygen cluster formation and the electronic modifications in the bulk. The impact of gold atoms deposited on ceria and their effect on the vacancy clusters are also discussed.

RESULTS AND DISCUSSION

XRD results

Lattice parameters of CeO_2 and 1%Au/CeO_2 (Figure 1, upper panel) clearly show lattice expansion as a consequence of oxygen evolution from the bulk, as expected in reducing conditions, and confirm the significant presence of Ce^{3+}. The effect of

CellPress
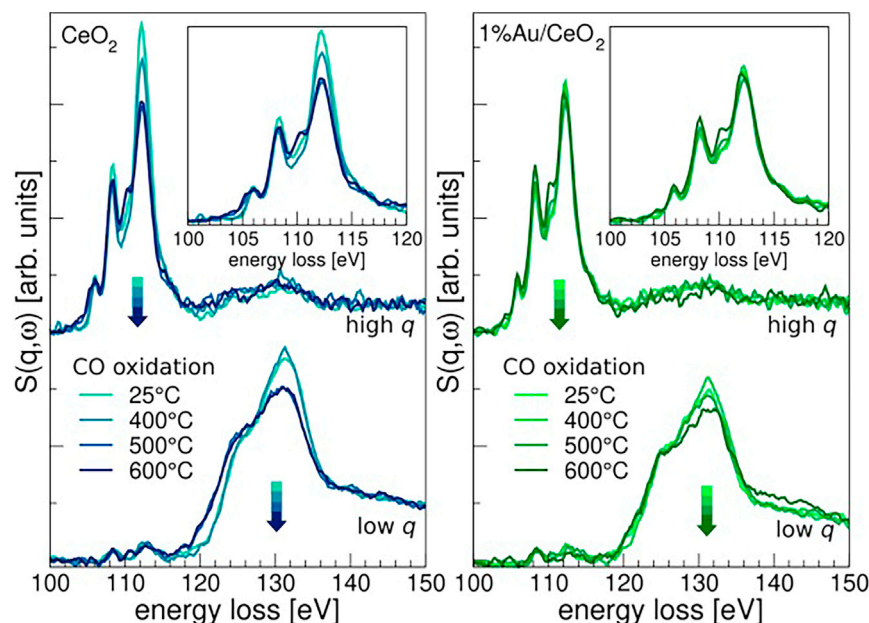OPEN ACCESS

**Cell Reports
Physical Science**
Article

Figure 2. Evolution of XRS spectra at different temperatures

Evolution of the Ce $N_{4,5}$-edges in the low-q and high-q ranges upon CO treatment at different temperatures for CeO_2 (left) and 1%Au/CeO_2 (right). The arrows show the evolution of the spectra upon CO oxidation with increasing temperature from 25°C to 600°C. The spectrum of fresh CeO_2 coincides with that one collected at 25°C after CO treatment. No differences were recorded.

thermal expansion alone ($\alpha = 1.271*10^{-6}°C^{-1}$[45]) is shown for comparison. Based on the error bar values for pure ceria, it can be concluded that the formation of Ce^{3+} is negligible in the examined temperature range and during the air treatment (red squares in Figure 1, upper panel). Upon CO oxidation, the cubic cell size of both CeO_2 and 1%Au/CeO_2 increase. More specifically, a stronger expansion is observed for 1%Au/CeO_2, compared with CeO_2, reaching 5.56 Å vs. 5.51 Å at 800°C.

The amount of Ce^{3+} was determined (see Figure 1, lower panel) as described in Marrocchelli et al.[46] Up to 200°C, the concentration of Ce^{3+} is negligible in all samples, increasing to nearly 25% in CeO_2 under CO flow at 800°C. The presence of gold nanoparticles enhances the formation of Ce^{3+}, reaching almost 50% for 1%Au/CeO_2 at 800°C. All XRD patterns are shown in the SI.

XRS Ce $N_{4,5}$-edges

The evolution of XRS spectra at the Ce $N_{4,5}$-edges in the low-q and high-q ranges upon CO treatment at different temperatures for pure CeO_2 and 1%Au/CeO_2 catalyst is shown in Figure 2. The spectra show that the non-dipole multiplet structure is highly sensitive to the redox treatment, having a clear impact on the 4f occupation. At low q values (3.5 Å^{-1}), the signals are dominated by the giant dipole resonance decreasing with q (i.e., beyond dipole approximation). At high q values (9.5 Å^{-1}), the contribution of the dipole resonance to the spectrum is greatly reduced, and the XRS spectra near the 4d binding energy are dominated by the pre-threshold peaks of the Ce 4f multiplet.[47,48]

As shown in Figure 2, variations in terms of peak intensity and position are observed upon CO exposure for both the low-q and high-q values for all samples, due to the formation of Ce^{3+} (electronic configuration 4f^1).[47,48] The formation of an oxygen

Cell Reports
Physical Science
Article

vacancy is accompanied by two polarons due to the transfer of two electrons from the O 2p states to Ce 4f states of two different cations. Therefore, the component of $Ce^{3+}(4f^1)$ increases during a reducing treatment with CO (see supplemental information file).[1,2,19,24,29,49–53]

Ligand-field atomic-multiplet calculations allow the description of atomic transitions in localized electronic systems and solids.[47] It is therefore possible to calculate the multiplet structure of core-to-4f excitations in rare earths elements to good agreement with experimental data.[47,48] The multiplet structure is very sensitive to the atomic environment, and strongly depends on the electronic structure of the atom undergoing the transition, which in this case is from 4d to 4f.

Following the approach of previous theoretical studies, simulated Ce $N_{4,5}$-edge spectra at different q are reported in Figure 3.[48] The calculated spectrum of CeO_2 exhibit only one peak at 130 eV, while the presence of Ce^{3+} is demonstrated by two peaks at 122 and 125 energy loss eV, respectively (see also supplemental information). However, irrespective of the momentum transfer, more than one peak is always visible in the experimental spectra of both the fresh CeO_2 and $1\%Au/CeO_2$ samples at 122 and 133 eV (Figure 3B). The main peak at 133 eV is due to Ce^{4+}, as further confirmed by simulations (see Figure 3A and the supplemental information). Since the Ce^{4+} contributions alone cannot reproduce all the spectral features at lower energies, a significant presence of Ce^{3+} must be taken into account for the samples after CO oxidation in accordance with the results from XRD presented above.[1,2,19,24,29,48–53] Thus, to calculate the XRS spectrum, both Ce^{3+} and Ce^{4+} signals are used and accordingly weighted up to get the best match to the experimental spectrum. As expected, upon CO treatment, the amount of Ce^{3+} increases by increasing the temperature.

The spectral modifications shown in Figure 2 and analyzed in Figure 3 can be summarized as follows: (1) at low q, a red shift in energy is evident, and the intensity of the main peak at 133 eV decreases; and (2) at high q, a small red shift in energy and changes to the peak ratio are visible (at 110 eV).

The multiplet simulations were then used to quantify the Ce^{3+} component, i.e., indirectly quantify the oxygen vacancies. The simulations from the XRS data are reported in Figure 3, and demonstrate that CeO_2 contains around 20% of Ce^{3+} after CO oxidation at 600°C (Figure 3D). The latter value is close to the one calculated from XRD at 600°C: Ce^{3+} was calculated around 15% (see Figure 1). Most importantly, the $1\%Au/CeO_2$ sample already contains around 10% of Ce^{3+} at room temperature (Panel Figure 2C). The amount of Ce^{3+} increases upon the reducing treatment reaching around 30%–35% at 600°C (Panel D).

These results highlight that (1) Ce^{3+} forms in ceria at 600°C upon CO oxidation, and (2) Ce^{3+} forms in Au/CeO_2 upon CO oxidation already at low temperature (below 150°C). Neither of these effects has been previously proposed based on earlier diffraction analysis (either X-ray or neutron). To understand this result, one must keep in mind that XRS probes every Ce^{3+} atom, while diffraction techniques are sensitive to average lattice variations only, so the surface Ce^{3+} formed by the direct interaction with the reducing gas does not impact the diffraction pattern. For sake of completeness, we investigated also the surface chemical composition of the samples by X-ray photoemission spectroscopy. The identification of Ce^{3+} species confirmed the presence of oxygen vacancies also in the surface layer (see the supplemental information).
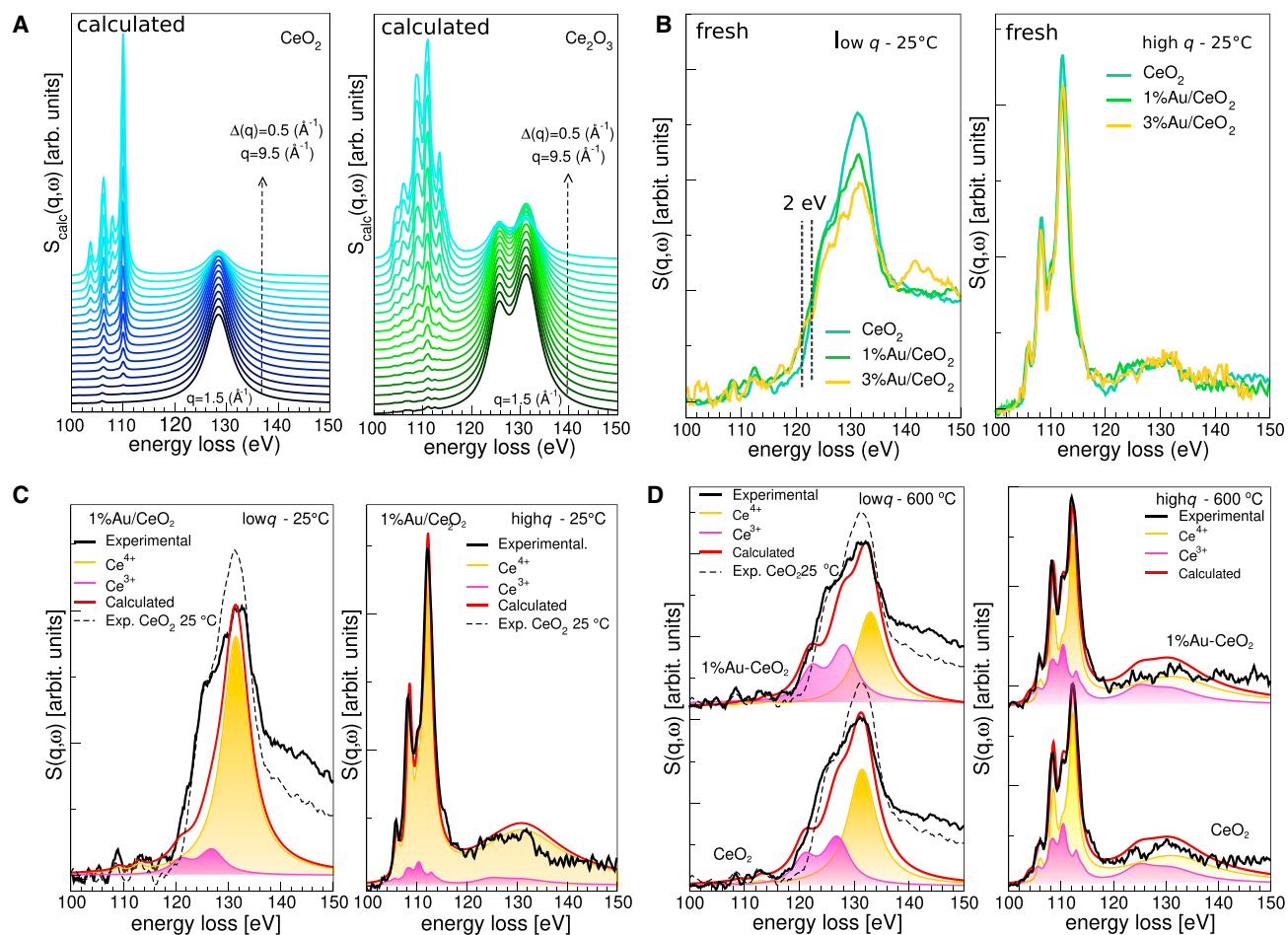
Figure 3. Simulated Ce $N_{4,5}$-edge spectra at different q

(A) The calculated spectra are compared: Multiplet simulations of the Ce $N_{4,5}$-edges XRS spectra at increasing q (1.5–9.5 $Å^{-1}$ bottom to top) for CeO_2 (left) and Ce_2O_3 (right).

(B) The experimental spectra at fresh state are compared: comparison of the Ce $N_{4,5}$ edges XRS spectra of CeO_2 (light blue), 1%Au/CeO_2 (light green) and 3%Au/CeO_2 (yellow) at low q (left) and high q (right) at 25°C. The vertical lines are a guide to the eye.

(C) The experimental Ce $N_{4,5}$ edge XRS spectra of 1%Au/CeO_2 and calculated spectra (red) at low q (left) and high q (right) at 25°C are compared.

(D) Experimental Ce $N_{4,5}$ edges XRS spectra of 1%Au/CeO_2 and calculated spectra (red) at low q (left) and high q (right) at 600°C are compared. In (C) and (D), the reference XRS spectrum of CeO_2 is also shown at low q (dashed line), together with the single contributions from Ce^{3+} (magenta) and Ce^{4+} (yellow).

The agreement obtained in the finer features of the high-q spectra depends essentially on the relative concentrations of Ce^{3+} and Ce^{4+}, and not on the details of the multiplet. Moreover, it is worth noting that the high-q multipole peaks are not affected by the interaction of the photoelectron with the continuum, which broadens the giant dipole resonances.

The results at high-q values are very stringent and robust: the formation of Ce^{3+} in Au/ceria occurs during CO oxidation even at low temperature (below 150°C).

XRS O K-edge

XRS measurements at the O K-edge are shown in Figure 4A. Three sharp peaks are evident at around 530.7 eV, 533.5 eV, and 537.9 eV and are assigned as 4f, 5d-e_g and 5d-t_{2g}, respectively: these are associated with unoccupied states originating from the O 2p hybridization with the Ce 4f and Ce 5d orbitals, split by the cubic
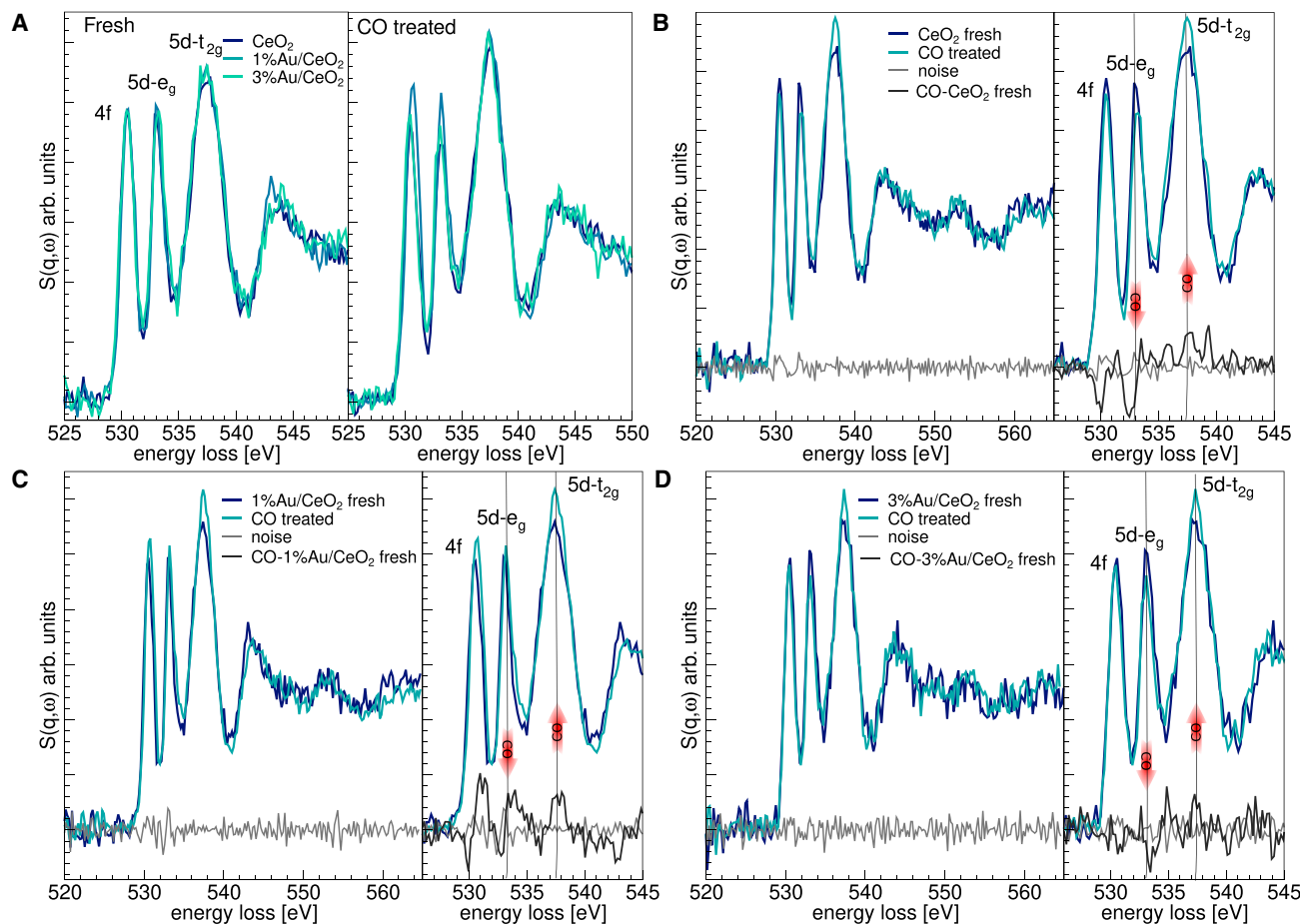
CellPress
OPEN ACCESS

Figure 4. Experimental XRS spectra at the O K-edge before and after CO treatment

(A) All fresh (left) and CO-treated (right) samples with or without Au.

(B) CeO_2.

(C) $1\%Au/CeO_2$.

(D) $3\%Au/CeO_2$. In (B)–(D), noise is plotted as the difference between raw and smoothed data. Difference between the CO-treated and the fresh sample is also reported in the aside inset of (B)–(D) (labeled CO treated – fresh). The arrows highlight the evolution of spectral features after CO treatment. The vertical lines are a guide to the eye.

crystal field.[39,48,50–53] As reported earlier, the splitting of the Ce 4f states is not detected due to the small overlap between the f orbitals and p orbitals of the oxygen.[39,52]

As evident in Figure 4A (left), no significant differences are detected in the O K-edge between the fresh samples with or without Au. However, clear changes are evident in all the XRS signals upon CO oxidation (Figures 4A, right, and 4D). The observed variations in the 5d-e_g and 5d-t_{2g} peak ratios and positions are found to be slightly dependent on the Au loading. The XRS spectra of the CO-treated samples show that both 5d-e_g (533 eV) and 5d-t_{2g} (538 eV) peaks are shifting to higher energy loss values (Figures 4B–D). The former peak intensity lowers, and the latter raises and broadens upon CO oxidation. The first peak at 530.7 eV, corresponding to the hybridization of Ce 4f orbitals with O 2p, also shifts slightly to higher energy.

The reported variation at the O K-edge is clearly small. This is not surprising, since the number of vacancies formation affect partially the ceria oxygen lattice modifying
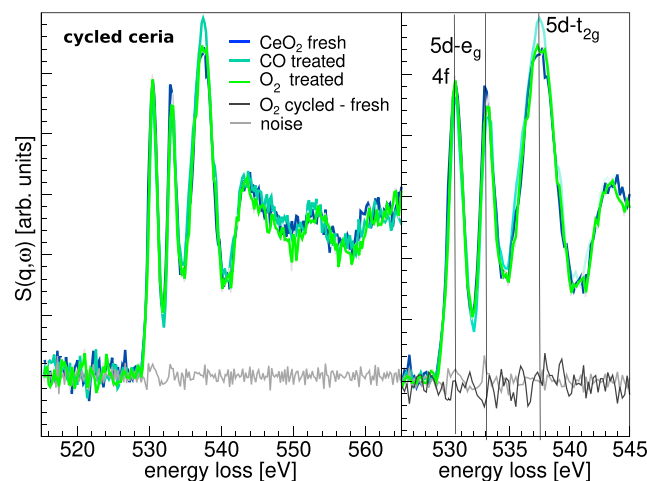
Figure 5. Experimental XRS spectra at the O K-edge of CeO_2
Spectra are fresh (blue), CO treated (turquoise), and O_2 treated (light green). The differences between O_2 and fresh samples are drawn in black (named O_2 cycled-fresh). The noise (gray) is the difference between raw data and smoothed signals. Right inset: enlargement of the peaks with assignments and differences between the O_2-treated and the fresh sample (black). The vertical lines are a guide to the eye.

only oxygen atoms closer to the defect. Moreover, only the average of the all oxygen atoms is measured. To prove the consistency of the differences and their reversibility, the CO-treated samples were re-exposed to oxygen at 650°C in order to oxidize Ce^{3+} to Ce^{4+}. After this reoxidation, as shown in Figure 5, all previous changes induced by the CO treatment are reversed. The modifications observed in the spectra indicate that the oxygen sublattice of ceria and its electronic structure undergo modifications as a result of the CO treatment. Therefore, the observed effects upon CO treatment cannot be explained solely by the variations occurring at the surface or subsurface of the oxide, and must involve the bulk. In fact, the attenuation length of 9.7 keV X-rays in CeO_2 is 1.3 µm at 10° incidence, and 8 µm at normal incidence, while the surface is several orders of magnitude thinner (only a few atomic layers).

Moreover, the results obtained from the analysis of the Ce $N_{4,5}$-edges also support this conclusion, as they suggest that ceria treated at 650°C exhibits a high density of lattice oxygen vacancies (see Figure 3). These observations provide a strong compelling motivation to simulate the effects of vacancy formation in the bulk.

Oxygen vacancies clusters
To elucidate the modifications of the hybridization of the 4f and 5d states shown in Figure 4, *ab initio* DFT calculations of pristine and defective ceria lattices were performed to assess their structure and energy. The oxygen-defective ceria lattices were built with a different number of isolated and clustered vacancies according to the scheme reported below. The idea that oxygen vacancies can cluster in the bulk stems from the earlier results that focused on the surface oxygen vacancies in CeO_2. Detailed descriptions of the cluster formation and their possible configurations are discussed in detail in the literature.[30–36,50–53]

Studies of CeO_2 surfaces, both by STM and *ab initio* calculations, show linear vacancy clusters at temperatures higher than 25°C[19,21,26,27,53] along the

Cell Reports
Physical Science
Article

CellPress
OPEN ACCESS

Table 1. Lattice parameter and stabilization energy (compared with C_0) of the relaxed structures reported in the text

Pure ceria	a (Å)	ΔE (eV)
C_0	5.5635	
C_R	5.5625	–
C_{-1}	5.5641	–
C_1	5.5668	+1.66
C_3	5.5778	+3.78
C_5	5.5830	+2.85
C_7	5.5854	+3.60

crystallographic [110] or [111] directions, with the Ce^{3+} ions in the vicinity of the vacancy, but only as next-nearest neighbors with $Ce^{3+}-O-V$ bridges. Thus, we modeled ceria structures containing vacancy clusters, starting from an ordered lattice of evenly spaced isolated oxygen vacancies, labeled C_0.[26,50–53] After creating the first vacancy site, further oxygen vacancies are created using a linear combination of the lattice vectors [220], [202], and [022] with integer coefficients, until a vacancy concentration of 12.5% is reached.[20–26] The stability of this lattice was then evaluated with respect to further modifications of the vacancy arrangement: (1) a disordered random arrangement of 24 oxygen vacancies (C_R); and (2) several C_n configurations built from C_0 with 24 + n oxygen vacancies, from n = −1 to n = 7 (full details are reported in the supplemental information). In particular, the configurations C_1, C_3, C_5, and C_7 contain a linear, tetrahedral, octahedral, and cubic cluster of vacancies, respectively. In structure C_1, one extra vacancy is created between two others, creating a trimer along the [110] direction, at second-neighbor distance intervals. This layout has been reported as one of the preferred modes of clustering, together with alignments along the [111] direction at third-neighbor distance intervals.[26–28] The structures C_3, C_5, and C_7 are then obtained by creation of three, five, and seven more vacancies, respectively. In C_3, two more vacancies are arranged in a tetrahedral cluster. The seven extra vacancies in C_7 are grouped together to form a cubic cluster. The C_5 structure is derived from C_7 by filling two vacancies of the cube, obtaining an octahedral vacancy cluster. To test the robustness of our results relatively to other choices of U ($5eV$[54] in our case) we calculated the C_7 system also at U = 4.5eV[55] finding a stabilization energy of 3.74 eV representing a 4% increase, which does not alter our conclusions.

The relaxed lattice parameters and energies of the different vacancy structures are reported in Table 1 (see the supplemental information for details). The calculations were also validated by comparison with a different calculation approach using VASP (see the supplemental information). The values of the lattice parameter agree with the expansion due to the formation of Ce^{3+} and are in agreement with the experimental values obtained by XRD for the samples measured upon CO oxidation.

The relaxed structures and the respective O K-edge XRS simulated spectra are shown separately in Figure 6, and further compared in Figure 7. The same trends previously observed after the CO treatment (i.e., the intensity lowering and energy shift of the d-t_{2g} peak, the strengthening of e_g), can be appreciated again in the simulations as the vacancy concentration increases. In particular, the d-t_{2g} peak also increases by moving from a linear ordering of vacancies to cubic clustering. The d-e_g peak slightly decreases with the clustering of vacancies, except for tetrahedral arrangement. Such effect of increased clustering in the bulk is also coherent with the analysis of the Ce $N_{4,5}$-edges discussed above.
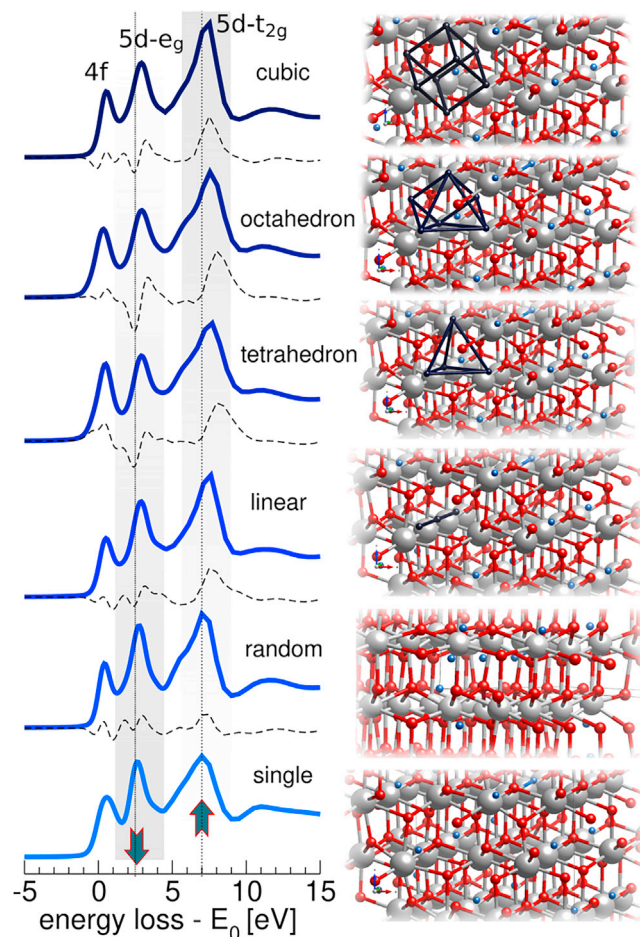
Figure 6. Theoretical O K-edge XRS spectra calculated at low q and their corresponding oxygen vacancy cluster structures

The oxygen atoms are drawn in red, the cerium atoms in gray, the single vacancies in blue, and the cluster vacancies are represented in dark blue. The vertical dotted lines highlight the position of the e_g, and t2g states. The dashed lines show the difference between each spectrum and the C_0 structure spectrum (bottom). The arrows indicate the modifications of the peaks in vacancies cluster spectra.

All these modifications are better appreciated in the difference spectra, obtained by subtracting the calculated XRS spectra to the reference spectrum of the C_0 structure, which is free of any oxygen vacancy clusters. The difference spectra then highlights that (1) the creation of oxygen vacancies clusters has an effect on the oxygen bulk lattice resulting in an evident modification of the hybridization of the 5d states; (2) the different arrangements of oxygen vacancies affect the intensity of the 5d-e_g and 5d-t_{2g} states, as witnessed by the changes in peak intensity and position; and (3) the peak shift is linked to both electronic and lattice structure rearrangement as a consequence of the reduction of cerium.

Interestingly, the formation of oxygen vacancy clusters is supported by several previous DFT+U works, corroborating the fact that the excess electron density after vacancy formation is localized on certain cation sites so that the coordination number of Ce^{3+} remains high.[26,30,31,49–53] In this view, oxygen vacancies are preferentially located away from Ce^{3+}, not in its first coordination shell. Of course, this tendency
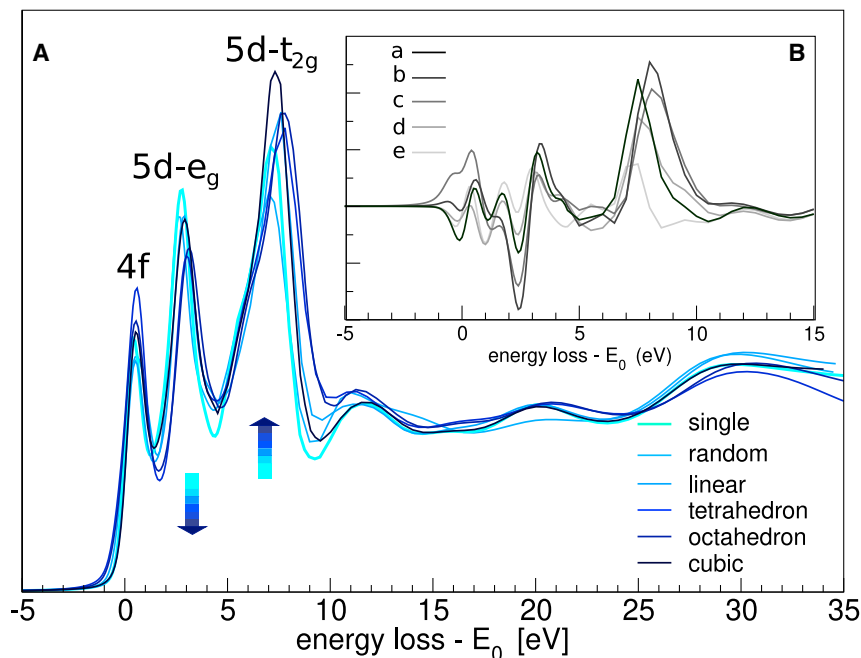
CellPress
OPEN ACCESS

Figure 7. Relaxed structures and the respective O K-edge XRS simulated spectra
(A) Comparison of the theoretical O K-edge XRS spectra at low q for each structure depicted in Figure 6, plotted in extended energy range.
(B) Comparison of the differences as defined in Figure 6. Curves a–e are the differences between the spectra of (a) cubic and C_0; (b) octahedron and C_0; (c) tetrahedron and C_0; (d) linear and C_0; and (e) random and C_0. The arrows indicate the modifications of the peaks in vacancies cluster spectra.

cannot be completely satisfied when the vacancy concentration is high, while it can be valid at lower vacancy concentrations.[30,31]

The role of gold atoms
Motivated by the results presented so far, we extended this approach to evaluate the impact of Au atoms on the ceria lattice, which contains oxygen vacancy clusters. In our model, we considered one gold atom placed inside a cluster of vacancies, reproducing an isolated gold atom in the ceria subsurface.[13–15,56,57] The structures that contain Au inside the vacancy clusters, as well as their respective stabilization energy values, are reported in the supplemental information (see Tables S1–S3 and Figure S8).

As is evident in Table S3, the entrapped gold has an important stabilization effect on the oxygen vacancies. Considering the representative case of a cubic oxygen vacancy cluster structure, obtained from an ideal CeO_2 crystal by removing eight oxygen atoms, the charge density contributed by the 16 uppermost occupied orbitals is shown in Figure 8. This density corresponds to the electrons donated by the formation reaction $O^X_O = V^{\cdot\cdot}_O + 2e^- + 1/2\ O_2(g)$ of the eight vacancies in the structure. Both panels have the same threshold value for the isosurface, and Figure 8B shows a slight inflation of the charge blob, outside of the drawn cube, which still remains localized. This localization is in agreement with a previous study.[25] The interaction of this excess charge with the embedded gold atom stabilizes the structure and its effect can be highlited by a Bader charges analysis of the surrounding ions.[58–63]

The six Ce ions that are close to the faces of the vacancies cube have a Bader charge of 10.2 valence electrons each (the pseudopotential used for Ce has 12 valence
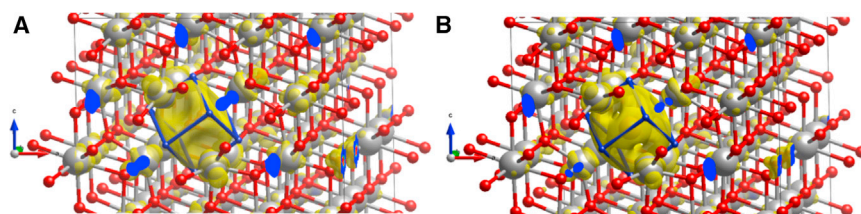
Figure 8. Charge density contributed by the 16 uppermost occupied orbitals of a CeO$_2$ supercell with a cubic vacancies cluster
(A) Charge density contributed by the 16 uppermost occupied orbitals of a CeO2 supercell with a cubic vacancies cluster. Oxygen atoms in red and their electronic density in yellow (blue in the isosurface cutting). The cerium atoms are drawn in gray.
(B) The same structure as in (A), after addition of a gold atom inside the vacancies cluster.

electrons) while all the other Ce ions have a Bader charge that oscillates very close to 9.5 electrons. After the introduction of the gold atoms, the Bader charge of the six neighboring Ce ions decreases down to the values of 9.8 valence electrons without major modifications for the other Ce ions. The Bader charge of the gold atom is 13.8 valence electrons instead, to be compared with the value of 11 electrons in the pseudopotential.

Interestingly, apart from the energy stabilization discussed so far, no significant changes are observed in the calculated O K-edge XRS spectra with or without gold.

Despite the very different temperatures used for the CO oxidation in ceria (650°C) and Au/ceria (150°C) samples, comparable changes in the 5d-t_{2g} and 5d-e_g peak ratios, as well as their energy positions, are observed in their experimental O K-edge spectra. The latter highlights that similar modifications are occurring in the oxygen sublattice, which do not only depend on the temperature used. This observation aligns with the fact that Au is a highly active catalyst in the oxidation of CO. In fact, the formation of oxygen vacancy clusters in Au-supported catalysts follows a similar mechanism compared with what is observed in ceria alone, the only difference being the lower temperature.

A possible correlation between the CO oxidation and the clustering of oxygen vacancies can be inferred by directly comparing the difference spectra obtained by subtracting the CO-treated and pristine experimental spectra (see Figure 4) and the difference calculated from the simulated spectra. These are obtained by subtracting the spectrum of a cluster-containing structure from the C_0 reference configuration (see Figure 7, inset II).

From the comparison of the above-defined difference spectra, we can eventually determine the extent of electronic modification that occurs during the CO treatment and how it relates to the formation of oxygen vacancy clusters. Ideally, the spectra of the models and their difference should be able to differentiate among the various vacancy cluster arrangements; however, the comparison mainly allows for distinguishing between oxygen clusters and isolated vacancies (see Figure 7).

To simplify this analysis, we then defined a difference spectrum considering an average of all oxygen vacancy clusters and subtracting the C_0 reference configuration. The direct comparison with the experimental differences is shown in Figure 9. For comparison, the difference spectrum obtained by subtracting C_R from
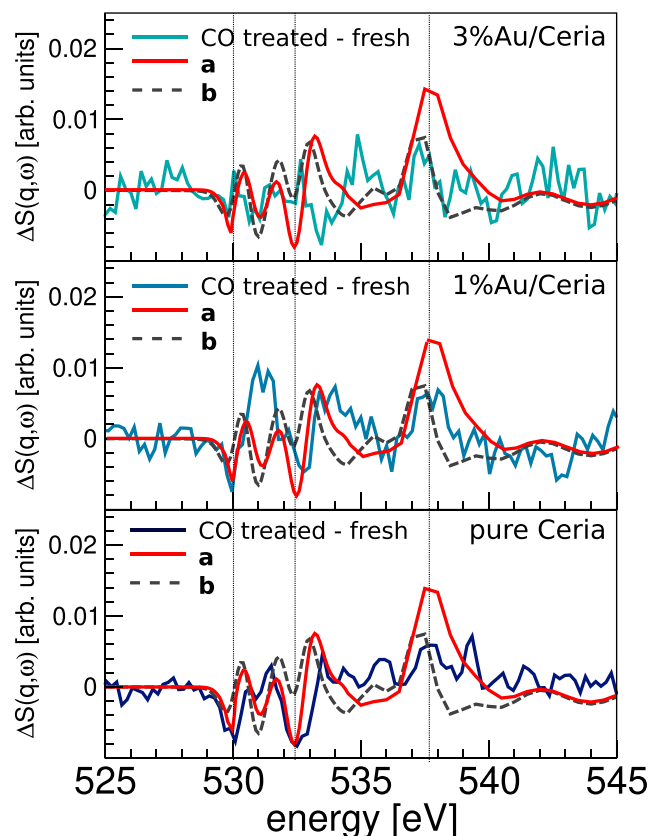
**Cell Reports
Physical Science**
Article

CellPress
OPEN ACCESS

Figure 9. Difference spectra

Difference spectra are shown for for pure ceria (bottom), 1%Au/CeO$_2$ (middle), and 3%Au/CeO$_2$ (top). The experimental difference spectra indicated as CO treated-fresh (in turquoise, blue, and dark blue) are compared with the model differences spectra a (red) and b (dashed line), where a is the difference between the average of the vacancy clusters and C$_0$, and b is C$_R$ − C$_0$.

C$_0$ is also drawn, illustrating the effect of vacancy ordering alone, without clustering.

Based on a comparison of spectral features evidenced in Figure 9 (i.e., the position and intensity of minima and maxima), it can be inferred that ceria reasonably fits the model that considers a distribution of oxygen vacancies cluster, while 1%Au/CeO$_2$ can be described as a distribution of oxygen vacancy clusters and a random arrangement of isolated vacancies. On the other hand, the 3%Au/CeO$_2$ appears to be better described by random isolated vacancies only. The approach discussed so far allows us to prove the direct link between the electronic modification in the bulk structure due to CO treatment, and the formation of oxygen vacancy clusters in the bulk. This also clarifies how the metal loading impacts the vacancy cluster formation. Keeping in mind the different temperatures used in the experiments, we argue that in pure ceria and in 1%Au/CeO$_2$ the lattice gains stability when vacancy clusters are formed. On the other hand, in agreement with previous experimental evidence,[64–66] changes in the metal loading affect the ability of the whole lattice to accommodate isolated vacancies and make them more available also at low temperatures.

We investigated the clustering of oxygen vacancies in bulk CeO$_2$ by coupling XRD and XRS measurements with DFT and multiplet simulations. This combination of

experimental and modeling analysis allowed us to monitor the variation of the Ce^{3+} upon CO oxidation during *in situ* XRS: 20% of Ce^{3+} forms in pure ceria at 600°C, while Ce^{3+} exists in Au/CeO_2 even at low temperature (below 150°C), reaching 35% at 600°C. The formation of Ce^{3+} in the lattice of all the examined samples after CO oxidation is reversible, as demonstrated by the XRS spectra after O_2/He reoxidation at 650°C.

The XRS measurements at the O K-edge demonstrated that the clustering of oxygen vacancies is not limited to the surface level, but also involves the bulk of the reducible oxide. The variations of the O K-edge features, involving the modification of the Ce 5d peaks, were reproduced with a model that takes into account the increase of bulk oxygen vacancies, upon CO oxidation, and the consequent formation of vacancy clusters. These structures, confirming previous hypotheses, are the most stable structures in the case of high vacancy concentration. When the concentration of vacancies is low, they are not located in the first coordination shell of Ce^{3+}, but reside preferentially at longer distances.

The loading of the active metal (i.e., Au) deposited on CeO_2 impacts the structuring of lattice oxygen vacancies: 1% Au induces clustering in the oxygen vacancies, while 3% Au produces a random arrangement of vacancies. The latter can be ascribed to the ability of the whole lattice to accommodate isolated vacancies, even at low temperatures, when a higher metal loading (i.e., 3%) is available.

EXPERIMENTAL PROCEDURES

Resource availability

Lead contact
Information and requests for resources and materials should be directed to the lead contact, Alessandro Longo (alessandro.longo@cnr.it; alessandro.longo@esrf.fr).

Materials availability
This study did not generate new unique reagents.

Data and code availability
The experimental raw data of XRD and XRS experiments is deposited at the ESRF data portal, along with additional experimental results of surface and bulk analysis by at https://data.esrf.fr/doi/10.15151/ESRF-DC-1375603773. The Hilbert++ code is available from the corresponding authors upon reasonable request. Any additional information required to reanalyze the data reported in this paper is available from the lead contact upon request.

Materials synthesis
CeO_2 (Sigma-Aldrich, 60 m^2/g) was used as received and as support for the gold catalyst synthesis. Au/CeO_2 powders, with nominal loading of 1 and 3 wt % (as confirmed by ICP-AES), were prepared by a homogeneous deposition method reported elsewhere,[64–66] using urea as precipitating agent. The suspension was kept at 80°C for 16 h under stirring, until a pH value of ~7 was reached. The obtained solid was then filtered and washed repeatedly with water until no chloride ions were detected by the $AgNO_3$ test. The sample was eventually dried in static air at 120°C for 24 h. The resulting powder is labeled as "fresh" sample in the following.

X-ray Raman scattering
All XRS data were collected at the beamline ID20 of the ESRF. The pink beam from three U26 undulators was monochromatized, using a cryogenically cooled Si (111)

**Cell Reports
Physical Science
Article**

monochromator and focused to a spot size of approximately 50 μm × 50 μm (V × H) at the sample position using a mirror system in Kirkpatrick-Baez geometry. The large solid angle spectrometer at ID20 was used to collect XRS data with 36 spherically bent Si(660) analyzer crystals.[67] The data were treated with the XRStools program as described elsewhere.[68] The powder samples were pressed into pellets, which were placed at an angle of 10° with respect to the incident beam. The incident energy was 9.6789 keV, which corresponds to the elastic peak of the crystal analyzers. Full-range scans were measured from 0 to 700 eV energy loss with a 1 eV step size. After acquisition of the broad scan, several detail scans at specific edges were collected with a 0.2 eV step by scanning the O K-edge in the 520–590 eV energy loss range. The Ce $N_{4,5}$-edges (4d–4f transitions) were collected in the 95–150 eV energy loss range. Acquisition scans lasted around 6–8 h per sample including all edges. All scans were checked for consistency and signals from analyzer crystals at different scattering angles (low-, medium-, and high-q) were measured simultaneously, spanning a momentum transfer from 2.5 to 9.2 $\pm$ 0.4 Å^{-1}. The overall energy resolution was 0.7 eV as estimated from the FWHM of elastic scattering of adhesive tape.

All XRS measurements were collected using the high-temperature *in situ* furnace for microtomography developed at ESRF. For the O K-edge, each sample underwent a redox cycle as reported in the literature for previous HERFD-XANES experiments performed at the Au L_3-edge.[65] Each redox cycle consists of a consecutive catalyst exposure to CO (1 vol % in He) for 120 min and O_2 (20 vol % in He) for 60 min at each temperature (from 25 up to 800°C). Before starting the reduction and before exposing the catalyst to oxygen, the cell was flushed with He for 30 min. In all reactions, the gas flow was 20 mL/min. The measurements were performed on the pristine sample before starting the treatment and in between the two redox cycles. In order to improve the signal-to-noise-ratio, the spectra of the oxygen K-edge were collected at room temperature after each treatment. All the measurement signals were stable in time during each measurement phase.

X-ray diffraction

In situ X-ray diffraction experiments, were carried out at ID20 in combination with the XRS measurements at 10.16 keV (λ = 1.22 Å). The XRD patterns were collected in reflection mode with a Pilatus 300K-W detector (1475 × 195 pixels of 172 × 172 μm) set at a distance of 600 mm. The integration time for each measurement was limited to 10 s to avoid saturation of the detector. CeO_2 and α-Al_2O_3 standards (from NIST) were used to calibrate the scattering 2θ angles and the sample-to-detector distance of 598 mm. Rietveld refinements were performed with the GSASII software.[69]

Computational methods: DFT

As all measured signals were stable in time, we assumed thermodynamic equilibrium for each sequence. Accordingly, we considered several possible structures and studied their relative energetic stability. The *ab initio* calculations were performed within the DFT, plane wave basis set, and pseudo-potentials framework as implemented in Quantum Espresso (QE).[70,71] The VASP code was also used for comparison reasons.[72–75]

For the QE calculations, we used projector-augmented-wave (PAW) pseudo-potentials from the QE website for O and Au. For Ce, we generated a PAW pseudopotential with 12 valence electrons and a small pseudization radius for the core correction equal to 0.7 au, which is smaller than the radius of the maximum of the 4f radial wavefunction. The parameter choices for the Ce pseudopotential were driven by the aim

of properly treating the semi-core nature of the 4f orbitals and determined the hardness of the required kinetic cutoff energy for the wave-function (100 Ry) and of the charge and potential (830 Ry). For the VASP LDA+U calculations, we used the PAW pseudo-potentials provided with the VASP package with their default suggested energy cutoff of ~30 Ry for the wavefuctions and ~60 Ry for the augmentation charge.

The Perdew-Burke-Ernzerhof exchange-correlation function was used for all pseudo-potentials.[76,77] For the Ce atoms, the Hubbard repulsion term was set to U = 5 eV for 4f electrons.[54] All the initial atomic arrangements were obtained starting from a CeO_2 super cell consisting of 96 Ce and 192 O, with the a, b, c axes aligned along the [011], [211], and [111] directions, respectively, and adding oxygen vacancies and Au atoms. The relaxation procedure was performed without spin polarization and with a Marzari-Vanderbilt smearing for a temperature T_{smear} = 0.3 eV, relaxing ionic position and cell parameters to attain forces strength lower than 10^{-4} Ry/au. All the structures were relaxed computing the ground state energy. All the calculations were performed at the Γ point.

Computational methods: XRS simulations

The DFT-relaxed structures were used to calculate the XRS spectra with the FDMNES software package.[78,79] The XRS simulations of the O K-edge were performed by using non-relativistic multiple scattering theory based on the muffin-tin approximation for the potential shape of the Green scheme, with Hedin-Lundqvist exchange potential. The muffin-tin radii were fine-tuned to have a good overlap between the different spherical potentials. The approximation of non-excited absorbing atoms was used, which, in this case, better reproduces the experimental data.[78,79] The crystal and occupancy options available in the code were adopted to simulate the spectra.

Computational methods: Multiplet analysis

In order to quantify the Ce^{3+} component from the XRS spectra, the multiplet approach was adopted with the Hilbert++ code.[80] A full description of the underlying theory and its numerical procedure is reported elsewhere.[81] The method allows to take into account the q-dependence of d-d and d-f excitations and to evaluate the pre-threshold resonances outside of the dipole limit, as reported in previous studies.[81] To analyze the XRS spectra, calculations at the Ce $N_{4,5}$-edges were performed for the two ionic configurations Ce^{3+} (initial state $4d^{10} 4f^1$) and Ce^{4+} ($4d^{10} 4f^0$).

To simulate the spectrum of ceria, Ce^{4+} was surrounded by eight oxygens according to the *Fm-3m* crystallographic arrangement of CeO_2. On the other hand, for the spectrum of Ce^{3+} only seven oxygens were placed around the trivalent cation. In this case, the *P-3m1* space group arrangement of the Ce_2O_3 was assumed. For consistency, the energy position and the shape of both Ce^{3+} and Ce^{4+} components were fixed at the value obtained from the analysis of the references (see the supplemental information).

SUPPLEMENTAL INFORMATION

Supplemental information can be found online at https://doi.org/10.1016/j.xcrp.2023.101699.

CellPress
OPEN ACCESS

AUTHOR CONTRIBUTIONS

Conceptualization, A.L. and F.G.; Methodology, A.L. and A.M.; Investigation, A.L., A.M., E.D.C.G., C.J.S., M.P.C., L.A., S.A.T., F.G.; Writing – Original Draft, A.L. and A.M.; Writing – Review & Editing, A.L., A.M., S.A.T., and F.G.; Supervision, A.L. and F.G.

DECLARATION OF INTERESTS

The authors declare no competing interests.

INCLUSION AND DIVERSITY

We support inclusive, diverse, and equitable conduct of research.

REFERENCES

1. Trovarelli, A. (1996). Catalytic Properties of Ceria and CeO2-Containing materials. Chem. Rev. *38*, 439–520.

2. Trovarelli, A. (2002). Catalysis by Ceria and Related Materials (Imperial College Press).

3. Diwell, A.F., Rajaram, R.R., Shaw, H.A., and Treux, T.J. (1991). The role of ceria in three-way catalysts, in Catalysis Automotive Pollution Control. In Studies in Surface Science and Catalysis, 71 (Elsevier), pp. 139–152. 71st edn.

4. Haruta, M., Kobayashi, T., Sano, H., and Yamada, N. (1987). Novel Gold Catalysts for the Oxidation of Carbon Monoxide at a Temperature far below 0° C. Chem. Lett. *405*, 408.

5. Fu, Q., Saltsburg, H., and Flytzani-Stephanopoulos, M. (2003). Active nonmetallic Au and Pt species on ceria-based water-gas shift catalysts. Science *301*, 935–938.

6. Fu, X.P., Guo, L.-W., Wang, W.-W., Ma, C., Jia, C.J., Wu, K., Si, R., Sun, L.D., and Yan, C.H. (2019). Direct Identification of Active Surface Species for the Water−Gas Shift Reaction on a Gold−Ceria Catalyst. J. Am. Chem. Soc. *141*, 4613–4623.

7. Barakat, T., Rooke, J.C., Genty, E., Cousin, R., Siffert, S., and Su, B.L. (2013). Gold Catalysts in Environmental Remediation and Water-Gas Shift Technologies. Energy Environ. Sci. *6*, 371–391.

8. Martorana, A., Deganello, G., Longo, A., Prestianni, A., Liotta, L., Macaluso, A., Pantaleo, G., Balerna, A., and Mobilio, S. (2004). Structural evolution of Pt/ceria–zirconia TWC catalysts during the oxidation of carbon monoxide. J. Solid State Chem. *177*, 1268–1275.

9. Melchionna, M., and Fornasiero, P. (2014). The role of Ceria-Based Nanostructured Materials in Energy Applications. Mater. Today *17*, 349–357.

10. Montini, T., Melchionna, M., Monai, M., and Fornasiero, P. (2016). Fundamentals and Catalytic Applications of CeO2 -Based Materials. Chem. Rev. *116*, 5987–6041.

11. Mars, P., and van Krevelen, D.W. (1954). Oxidations Carried Out by Means of Vanadium Oxide Catalysts. Chem. Eng. Sci. *3*, 41–59.

12. Widmann, D., and Behm, R.J. (2014). Activation of Molecular Oxygen and the Nature of the Active Oxygen species for CO Oxidation on Oxide Supported Au Catalysts. Acc. Chem. Res. *47*, 740–749.

13. Wang, Y.G., Mei, D., Glezakou, V.A., Li, J., and Rousseau, R. (2015). R., Dynamic Formation of Single-Atom Catalytic Active Sites on Ceria-Supported Gold Nanoparticles. Nat. Commun. *6*, 6511–6519.

14. Guo, L.W., Du, P.P., Fu, X.P., Ma, C., Zeng, J., Si, R., Huang, Y.Y., Jia, C.J., Zhang, Y.W., and Yan, C.-H. (2016). Contributions of Distinct Gold Species to Catalytic Reactivity for Carbon Monoxide Oxidation. Nat. Commun. *7*, 13481–13489.

15. He, Y., Liu, J.C., Luo, L., Wang, Y.-G., Zhu, J., Du, Y., Li, J., Mao, S.X., and Wang, C. (2018). Size-Dependent Dynamic Structures of Supported Gold Nanoparticles in CO Oxidation Reaction Condition. Proc. Natl. Acad. Sci. USA *115*, 7700–7705.

16. Lohrenscheit, M., and Hess, C. (2016). Direct Evidence for the Participation of Oxygen Vacancies in the Oxidation of Carbon Monoxide over Ceria-Supported Gold Catalysts by using Operando Raman Spectroscopy. ChemCatChem *8*, 523–526.

17. Frost, J.C. (1988). Junction Effect Interactions in Methanol Synthesis Catalysts. Nature *334*, 577–580.

18. Li, Y., Li, S., Bäumer, M., Ivanova-Shor, E.A., and Moskaleva, L.V. (2020). What Changes on the Inverse Catalyst? Insights from CO Oxidation on Au-Supported Ceria Nanoparticles Using Ab Initio Molecular Dynamics. ACS Catal. *10*, 3164–3174.

19. Esch, F., Fabris, S., Zhou, L., Montini, T., Africh, C., Fornasiero, P., Comelli, G., and Rosei, R. (2005). Electron Localization Determines Defect Formation on Ceria Substrates. Science *309*, 752–755.

20. Sun, C., Li, H., and Chen, L. (2012). Nanostructured ceria-based materials: synthesis, properties, and applications. Energy Environ. Sci. *5*, 8475–8484.

21. Campbell, C.T., and Peden, C.H.F. (2005). Chemistry - Oxygen Vacancies and Catalysis on Ceria Surfaces. Science *309*, 713–714.

22. Fukui, K.i., Namai, Y., and Iwasawa, Y. (2002). Imaging of surface oxygen atoms and their defect structures on CeO2 (111) by noncontact atomic force microscopy. Appl. Surf. Sci. *188*, 252–256.

23. Namai, Y., Fukui, K.I., and Iwasawa, Y. (2003). Atom-resolved noncontact atomic force microscopic and scanning tunneling microscopic observations of the structure and dynamic behavior of CeO2 (111) surfaces. Catal. Today *85*, 79–91.

24. Torbrügge, S., Reichling, M., Ishiyama, A., Morita, S., and Custance, O. (2007). Evidence of subsurface oxygen vacancy ordering on

reduced CeO2 (111). Phys. Rev. Lett. *99*, 056101.

25. Jerratsch, J.F., Shao, X., Nilius, N., Freund, H.J., Popa, C., Ganduglia-Pirovano, M.V., Burow, A.M., and Sauer, J. (2011). Electron localization in defective ceria films: a study with scanning-tunneling microscopy and density-functional theory. Phys. Rev. Lett. *106*, 246801.

26. Ganduglia-Pirovano, M.V., Da Silva, J.L.F., and Sauer, J. (2009). Density-functional calculations of the structure of near-surface oxygen vacancies and electron localization on CeO 2 (111). Phys. Rev. Lett. *102*, 026101.

27. Ganduglia-Pirovano, M.V., Hofmann, A., and Sauer, J. (2007). Oxygen vacancies in transition metal and rare earth oxides: current state of understanding and remaining challenges. Surf. Sci. Rep. *62*, 219–270.

28. Fabris, S., Vicario, G., Balducci, G., De Gironcoli, S., and Baroni, S. (2005). Electronic and atomistic structures of clean and reduced ceria surfaces. J. Phys. Chem. B *109*, 22860–22867.

29. Zhang, C., Michaelides, A., King, D.A., and Jenkins, S.J. (2009). Oxygen Vacancy Clusters on Ceria: Decisive Role of Cerium f Electrons. Phys. Rev. B *79*, 075433.

30. Sutton, J.E., Beste, A., and Overbury, S.H. (2015). Origins and implications of the ordering of oxygen vacancies and localized electrons on partially reduced CeO2 (111). Phys. Rev. B *92*, 144105.

31. Murgida, G.E., Ferrari, V., Ganduglia-Pirovano, M.V., and Llois, A.M. (2014). Ordering of Oxygen Vacancies and Excess Charge Localization in Bulk Ceria: A DFT+U Study. Phys. Rev. B *90*, 115120.

32. Mehmood, R., Mofarah, S.S., Chen, W.F., Koshy, P., and Sorrell, C.C. (2019). Surface, Subsurface, and Bulk Oxygen Vacancies Quantified by Decoupling and Deconvolution of the Defect Structure of Redox-Active Nanoceria. Inorg. Chem. *58*, 6016–6027.

33. Luo, S., Li, M., Fung, V., Sumpter, B.G., Liu, J., Wu, Z., and Page, K. (2021). New Insights into the Bulk and Surface Defect Structures of Ceria Nanocrystals from Neutron Scattering Study. Chem. Mater. *33*, 3959–3970.

34. Matsukawa, T., Hoshikawa, A., and Ishigaki, T. (2018). Temperature-Induced Structural Transition of Ceria by Bulk Reduction Under Hydrogen Atmosphere. CrystEngComm *20*, 4359–4363.

35. Bansmann, J., Abdel-Mageed, A.M., Chen, S., Fauth, C., Häring, T., Kučerová, G., Wang, Y., and Behm, R.J. (2019). Chemical and Electronic Changes of the CeO2 Support during CO Oxidation on Au/CeO2 Catalysts: Time-Resolved Operando XAS at the Ce LIII Edge. Catalysts *9*, 785.

36. Abdel-Mageed, A.M., Chen, S., Fauth, C., Häring, T., and Bansmann, J. (2021). Fundamental Aspects of Ceria Supported Au Catalysts Probed by In Situ/Operando Spectroscopy and TAP Reactor Studies. ChemPhysChem *22*, 1302–1315.

37. Zhang, Y., Zhao, S., Feng, J., Song, S., Shi, W., Wang, D., and Zhang, H. (2021). Unraveling the Physical Chemistry and Materials Mcience of CeO2-Based Nanostructures. Chem *7*, 2022–2059.

38. Kopelent, R., van Bokhoven, J.A., Szlachetko, J., Edebeli, J., Paun, C., Nachtegaal, M., and Safonova, O.V. (2015). Catalytically Active and Spectator Ce3+ in Ceria-Supported Metal Catalysts. Angew. Chem. Int. Ed. *54*, 8728–8731.

39. Frati, F., Hunault, M.O.J.Y., and de Groot, F.M.F. (2020). Oxygen K-edge X-ray Absorption Spectra. Chem. Rev. *120*, 4056–4110.

40. Raimondi, G., Giannici, F., Longo, A., Merkle, R., Chiara, A., Hoedl, M.F., Martorana, A., and Maier, J. (2020). X-ray Spectroscopy of (Ba,Sr,La)(Fe,Zn,Y)O3−δ Identifies Structural and Electronic Features Favoring Proton Uptake. Chem. Mater. *32*, 8502–8511.

41. Longo, A., Theofanidis, S.A., Cavallari, C., Srinath, N.V., Hu, J., Poelman, H., Sabbe, M.K., Sahle, C.J., Marin, G.B., and Galvita, V.V. (2020). What Makes Fe-Modified MgAl2O4 an Active Catalyst Support? Insight from X-ray Raman Scattering. ACS Catal. *10*, 6613–6622.

42. Maslakov, K.I., Teterin, Y.A., Ryzhkov, M.V., Popel, A.J., Teterin, A.Y., Ivanov, K.E., Kalmykov, S.N., Petrov, V.G., Petrov, P.K., Farnan, I., and Farnan, I. (2018). The Electronic Structure and the Nature of the Chemical Bond in CeO2. Phys. Chem. Chem. Phys. *20*, 16167–16175.

43. Deganello, G., Giannici, F., Martorana, A., Pantaleo, G., Prestianni, A., Balerna, A., Liotta, L.F., and Longo, A. (2006). Metal−Support Interaction and Redox Behavior of Pt(1wt %)/Ce0.6Zr0.4O2. J. Phys. Chem. B *110*, 8731–8739.

44. Safonova, O.V., Guda, A.A., Paun, C., Smolentsev, N., Abdala, P.M., Smolentsev, G., Nachtegaal, M., Szlachetko, J., Soldatov, M.A., Soldatov, A.V., and van Bokhoven, J.A. (2014). Electronic and Geometric Structure of Ce3+ Forming Under Reducing Conditions in Shaped Ceria Nanoparticles Promoted by Platinum. J. Phys. Chem. C *118*, 1974–1982.

45. Ozawa, M., and Loong, C.-K. (1999). In situ X-ray and Neutron Powder Diffraction Studies of Redox Behavior in CeO2-Containing Oxide Catalysts. Catal. Today *50*, 329–342.

46. Marrocchelli, D., Bishop, S.R., Tuller, H.L., and Yildiz, B. (2012). Understanding Chemical Expansion in Non-Stoichiometric Oxides: Ceria and Zirconia Case Studies. Adv. Funct. Mater. *22*, 1958–1965.

47. Cowan, R.D. (1981). The Theory of Atomic Structure and Spectra (University of California Press).

48. Gordon, R.A., Seidler, G.T., Fister, T.T., Haverkort, M.W., Sawatzky, G.A., Tanaka, A., and Sham, T.K. (2008). High Multipole Transitions in NIXS: Valence and Hybridization in 4f systems. EPL *81*, 26004.

49. Sergentu, D.C., and Autschbach, J. (2022). X-ray Absorption Spectra of f-element Complexes: Insight from Relativistic Multiconfigurational Wavefunction Theory. Dalton Trans. *51*, 1754–1760.

50. Murgida, G.E., and Ganduglia-Pirovano, M.V. (2013). Evidence for Subsurface Ordering of Oxygen Vacancies on the Reduced CeO2 (111) Surface Using Density-Functional and Statistical Calculations. Phys. Rev. Lett. *110*, 246101.

51. Herper, H.C., Vekilova, O.Y., Simak, S.I., Di Marco, I., and Eriksson, O. (2020). Localized Versus Itinerant Character of 4f-States in Cerium Oxides. J. Phys. Condens. Matter *32*, 215502.

52. Duchoň, T., Aulická, M., Schwier, E.F., Iwasawa, H., Zhao, C., Xu, Y., Veltruská, K., Shimada, K., and Matolín, V. (2017). Covalent Versus Localized Nature of 4f Electrons in Ceria: Resonant Angle-Resolved Photoemission Spectroscopy and Density Functional Theory. Phys. Rev. B *95*, 165124.

53. Han, Z.K., Zhang, L., Liu, M., Ganduglia-Pirovano, M.V., and Gao, Y. (2019). The Structure of Oxygen Vacancies in the Near-Surface of Reduced CeO2 (111) Under Strain. Front. Chem. *7*, 436–512.

54. Andersson, D.A., Simak, S.I., Johansson, B., Abrikosov, I.A., and Skorodumova, N.V. (2007). Modeling of CeO2 Ce2O3 CeO2-x in the LDA+U formalism. Phys. Rev. B *75*, 035109.

55. Da Silva, J.L.F., Ganduglia-Pirovano, M.V., Sauer, J., Bayer, V., and Kresse, G. (2007). Hybrid Functionals Applied to Rare-earth Oxides: The Example of Ceria. Phys. Rev. B *75*, 045121.

56. Ta, N., Liu, J.J., Chenna, S., Crozier, P.A., Li, Y., Chen, A., and Shen, W. (2012). Stabilized Gold Nanoparticles on Ceria Nanorods by Strong Interfacial Anchoring. J. Am. Chem. Soc. *134*, 20585–20588.

57. Li, J., Guan, Q., Wu, H., Liu, W., Lin, Y., Sun, Z., Ye, X., Zheng, X., Pan, H., Zhu, J., et al. (2019). Highly Active and Stable Metal Single-Atom Catalysts Achieved by Strong Electronic Metal–Support Interactions. J. Am. Chem. Soc. *141*, 14515–14519.

58. Liu, J.C., Wang, Y.G., and Li, J. (2017). Toward Rational Design of Oxide-Supported Single-Atom Catalysts: Atomic Dispersion of Gold on Ceria. J. Am. Chem. Soc. *139*, 6190–6199.

59. Bader, R.F.W. (1998). Atoms in molecules. In Encyclopedia of Computational Chemistry (John Wiley & Sons, Inc)), p. 64.

60. Yu, M., and Trinkle, D.R. (2011). Accurate and Efficient Algorithm for Bader Charge Integration. J. Chem. Phys. *134*, 064111.

61. Tang, W., Sanville, E., and Henkelman, G. (2009). A grid-based Bader analysis algorithm without lattice bias. J. Phys. Condens. Matter *21*, 084204.

62. Sanville, E., Kenny, S.D., Smith, R., and Henkelman, G. (2007). An Improved Grid-Based Algorithm for Bader Charge Allocation. J. Comput. Chem. *28*, 899–908.

63. Henkelman, G., Arnaldsson, A., and Jónsson, H. (2006). A Fast and Robust Algorithm for Bader Decomposition of Charge Density. Comput. Mater. Sci. *36*, 354–360.

64. Casaletto, M.P., Longo, A., Venezia, A.M., Martorana, A., and Prestianni, A. (2006). Metal-Support and Preparation Influence on the Structural and Electronic Properties of Gold Catalysts. Appl. Catal., A *302*, 309–316.

Cell Reports
Physical Science
Article

CellPress
OPEN ACCESS

65. Longo, A., Liotta, L.F., Pantaleo, G., Giannici, F., Venezia, A.M., and Martorana, A. (2012). Structure of the Metal–Support Interface and Oxidation State of Gold Nanoparticles Supported on Ceria. J. Phys. Chem. C *116*, 2960–2966.

66. Longo, A., Giannici, F., Casaletto, M.P., Rovezzi, M., Sahle, C.J., Glatzel, P., Joly, Y., and Martorana, A. (2022). The Dynamic Role of Gold d-Orbitals During CO Oxidation Under Aerobic Conditions. ACS Catal. *12*, 3615–3627.

67. Moretti Sala, M., Martel, K., Henriquet, C., Al Zein, A., Simonelli, L., Sahle, C.J., Gonzalez, H., Lagier, M.-C., Ponchut, C., Huotari, S., et al. (2018). A High-Energy-Resolution Resonant Inelastic X-ray Scattering Spectrometer at ID20 of the European Synchrotron Radiation Facility. J. Synchrotron Radiat. *25*, 580–591.

68. Sahle, C.J., Mirone, A., Niskanen, J., Inkinen, J., Krisch, M., and Huotari, S. (2015). Planning, performing and analyzing X-ray Raman scattering experiments. J. Synchrotron Radiat. *22*, 400–409.

69. Toby, B.H., and Von Dreele, R.B. (2013). GSAS-II: the genesis of a modern open-source all purpose crystallography software package. J. Appl. Crystallogr. *46*, 544–549.

70. Giannozzi, P., Andreussi, O., Brumme, T., Bunau, O., Buongiorno Nardelli, M., Calandra, M., Car, R., Cavazzoni, C., Ceresoli, D., Cococcioni, M., et al. (2017). Advanced capabilities for materials modelling with Quantum Espresso. J. Phys. Condens. Matter *29*, 465901.

71. Giannozzi, P., Baroni, S., Bonini, N., Calandra, M., Car, R., Cavazzoni, C., Ceresoli, D., Chiarotti, G.L., Cococcioni, M., Dabo, I., et al. (2009). Quantum Espresso: a modular and open-source software project for quantum simulations of materials. J. Phys. Condens. Matter *21*, 395502.

72. Kresse, G., and Hafner, J. (1993). Ab initio molecular dynamics for liquid metals. Phys. Rev. B *47*, 558–561.

73. Kresse, G., and Hafner, J. (1994). Ab initio molecular-dynamics simulation of the liquid-metal-amorphous-semiconductor transition in germanium. Phys. Rev. B *49*, 14251–14269.

74. Kresse, G., and Furthmüller, J. (1996). Efficiency of ab initio total energy calculations for metals and semiconductors using a plane-wave basis set. Comput. Mater. Sci. *6*, 15–50.

75. Kresse, G., and Furthmüller, J. (1996). Efficient iterative schemes for ab initio total-energy calculations using a plane-wave basis set. Phys. Rev. B *54*, 11169–11186.

76. Perdew, J.P., Burke, K., and Ernzerhof, M. (1996). Generalized gradient approximation made simple. Phys. Rev. Lett. *77*, 3865–3868.

77. Perdew, J.P., Ernzerhof, M., Burke, K., and Burke, K. (1996). Rationale for mixing exact exchange with density functional approximation. J. Chem. Phys. *105*, 9982–9985.

78. Joly, Y. (2001). X-ray Absorption Near-Edge Structure Calculations Beyond the Muffin-Tin Approximation. Phys. Rev. B *63*, 125120.

79. Joly, Y., Cavallari, C., Guda, S.A., and Sahle, C.J. (2017). Full-potential simulation of X-ray Raman scattering spectroscopy. J. Chem. Theor. Comput. *13*, 2172–2177.

80. Mirone, A., Sacchi, M., and Gota, S. (2000). Ligand-field atomic-multiplet calculations for arbitrary symmetry. Phys. Rev. B *61*, 13540–13544.

81. Longo, A., Wernert, R., Iadecola, A., Sahle, C.J., Stievano, L., Croguennec, L., Carlier, D., and Mirone, A. (2022). An Original Empirical Method for Simulating V L2,3 Edges: The Example of KVPO4F and KVOPO4 Cathode Materials. J. Phys. Chem. C *126*, 19782–19791.